https://doi.org/10.1016/j.actamat.2017.06.061
This is the Pre-Published Version.

Stick-slip dynamics in a $Ni_{62}Nb_{38}$ metallic glass film during nanoscratching

D.X. Han[a], G. Wang[a,*], J.L. Ren[b,*], L.P. Yu[b], J. Yi[a], I. Hussain[a], S.X. Song[c], H. Xu[a], K.C. Chan[d], P.K. Liaw[e]

[a] Laboratory for Microstructures, Institute of Materials, Shanghai University, Shanghai 200444, China

[b] School of Mathematic and Statistics, Zhengzhou University, Zhengzhou 450001, China

[c] State Key Laboratory of Metal Matrix Composites, School of Materials Science and Engineering, Shanghai Jiao Tong University, Shanghai 200240, China

[d] Department of Industrial and System Engineering, The Hongkong Polytechnic University, Hongkong, China

[e] Department of Materials Science and Engineering, The University of Tennessee, Knoxville, TN 37996 USA

Corresponding authors: g.wang@i.shu.edu.cn (G.W.) and renjl@zzu.edu.cn (J.L.R.)

Abstract

Stick-slip dynamics during nanoscratching is investigated for the $Ni_{62}Nb_{38}$ metallic glass. Detrended fluctuation analysis is introduced to explore the influence of loading force on the temporal scaling and stick-slip behavior. The self-similar characteristics and complexity in the temporal scale of the lateral force signal are investigated. A modified Cauchy class model is used for the stochastic stick-slip process, which connects the fractal dimension and the Hurst exponent and features the positive correlation process. The confidence intervals of the differential friction coefficient at different loading forces elucidate the inhomogeneous (and homogeneous) shear-branching processes during the nanoscratching process.

Keywords: stick-slip dynamics; metallic glass film; nanoscratching; self-similar behavior; fractal dimension

1. Introduction

Friction is of great importance in the industrial applications of metals, and occurs at different levels, including micro-electro-mechanical systems (MEMS) on the nanoscale, machining of metallic surfaces on the microscale, and rock avalanching on the macroscale [1–5]. Continuous miniaturization of machining processes of metallic surfaces towards the nanoscale, i.e., approaching nanoscratching [6], can provide insights on the investigation of friction, wear, and chip-separation behavior of metals on the nanoscale, leading to effective measures to reduce friction, improve the quality of the machined surface, and promote the service reliability of mechanical systems [7,8]. The friction is usually manifested in a stick-slip behavior [9–11]. Thus, probing the stick-slip dynamics during friction (or nanoscratching) is a key point in understanding the mechanism of friction behavior. Furthermore, during friction, stick-slip behavior actually reflects a surface damage process that is associated with an intermittent deformation process underlying lateral force. Therefore, the investigation of the surface damage process or the intermittent deformation process during the nanoscratching process may provide valuable information for understanding the damage process of metals underlying lateral force.

In the present study, a $Ni_{62}Nb_{38}$ (atomic percent, at. %) metallic glass is chosen as the model material for nanoscratching experiments because metallic glasses are potentially structural materials due to their high strength, good anti-corrosion ability, high hardness, etc. [12–17]. $Ni_{62}Nb_{38}$ metallic glass has an advantage in forming nanosized surface roughness and an accurate shape to the submicron scale for its high fracture strength (≈3.1 GPa) [18]. Thus, $Ni_{62}Nb_{38}$ metallic glass is a potential application material for the thermo-forming moulds that can be used in the fabrication of functional optical components [19].

With the high spatial and temporal resolution from nanoscratching, stick-slip behavior during the nanoscratching process can be investigated [20]. The stick-slip dynamics has been widely investigated in compressive deformation [21,22], during which the intermittent plastic-strain burst was analyzed using various methods, such as chaotic-time-series analysis [23], statistical analysis [24,25], and the spatiotemporal dynamic model [26,27]. These previous studies confirmed the agreement between the high-temporal-resolution measurements of the slip dynamics and the predictions of a simple mean-field theory [28], and shed light on the concept that the large ratio between laterally and vertically growing slip steps in the slip dynamics could lead to the discrepancy between collective dislocation velocities and measured slip velocities [29]. However,

so far, the dynamic behavior of nanoscratching in metallic glasses has not been given much attention. In the current study, detrended fluctuation analysis is used to explore the stick-slip process during the nanoscratching of metallic glass. A metallic glass film was used to guarantee a smooth surface for nanoscratching).

2. Experimental methods

The $Ni_{62}Nb_{38}$ metallic glass films that were unrelaxed glassy states were deposited on a cleaned monocrystalline silicon wafer with a size of 10×10×0.5 mm, in a high-vacuum chamber (a base pressure of 5×10^{-5} mbar) with a load-lock system, and a probe handler by means of a direct current (DC) planar magnetron sputtering device (Shenyang ZKY Technology Development Co., JGP-450). The chamber pressure was kept constant by an adaptive pressure controller during film deposition. The films were deposited without external heating, the sputtering time was 4 hours, and the sputtering power was 60 W. The thickness of the $Ni_{62}Nb_{38}$ metallic glass film was approximately 2 μm, measured from a cross-section view observed by high-resolution scanning electron microscopy (SEM) (Phenom world, Phenom Proxy).

Nanoscratching experiments were conducted in a Triboindentor TI-900 machine (Hysitron, Inc.). The nanoscratch indentor was a conic diamond with a tip radius of 1 μm and a half-angle of $\pi/6$. The initial tip-shape calibration was tested by a pure aluminum single crystal. Load force and displacement resolution were 50 nN and 2×10^{-2} nm, respectively. The scratch length was 20 μm, and the moving speed of the nanoindentor was 2 μm/s. Nanoscratch testing was conducted at different loading forces of 500, 1000, 1500, and 2000 μN in order to study the effect of loading force on the nanoscratching process of the metallic glass. At each loading force, at least four scratches were repeatedly performed. To obtain the background noise, an air-scratch test was also performed. After nanoscratch testing, the amorphous nature of the $Ni_{62}Nb_{38}$ film was confirmed by the glancing-incidence X-ray-diffraction technique (GIXRD) [30,31] with Cu *K*α radiation at a 1.5° angle of incidence to the specimen surface in a D/max-2200 X-ray diffractometer (Fig. 1). The scratching morphology was observed by SEM and an atomic force microscope (AFM) (Bruker Scientific Instruments, Multimode 8).

3. Results

Before the experiments, it was necessary to determine the background noise from the machine

vibration. Scratching in air was carried out. The lateral force, F_L, i.e., the force pushing the indentor slipping in the air, as a function of scratch length, is shown in Fig. 2(a). Enlarging the lateral force–scratch-length curve that is enclosed in the rectangle in Fig. 2(a), we see that the amplitudes of the lateral force fluctuation are approximately 3.84 μN, which corresponds to the background noise, as shown in Fig. 2(b). Therefore, the lateral force fluctuations within 3.84 μN are excluded in the following analysis to eliminate the influences from the background noise.

To clearly describe the nanoscratching process, Fig. 3 representatively plots the loading force, F_N, lateral displacement, S_L, and normal displacement, S_N, as functions of time, t, at a loading force of 1000 μN. According to the F_N-t curve, seven stages are distinguished. The first stage is from 0 to 4 s, in which the nanoindentor moves to the surface of the metallic glass film, and the F_N value is zero. From 4 to 9 s, i.e., the second stage, the nanoindentor tip touches the surface of the film, and penetrates into the metallic glass, in which, with increasing F_N value, the S_N value increases, but the S_L value does not significantly change. In the third stage (from 9 to 12 s), the F_N and S_L values are almost kept constant, and the S_N value slightly moves into the film. In this stage, the nanoscratching has not really started. After that, the nanoscratching process that is the subject of investigation occurs in the time duration from 12 to 22 s (fourth stage), which is enlarged and shown in the inset of Fig. 3. From 22 to 30 s (fifth stage), the scratching process is finished. In the following analysis, the nanoscratching process in the fourth stage will be investigated. The loading force leads to the creep behavior that is unstable at the initial time window of 0–3 s in the fourth stage, i.e., 12–15 s in the entire loading window, will be excluded, which is shown in Fig. 4.

The lateral force pushing the indentor slipping on the $Ni_{62}Nb_{38}$ metallic glass film as a function of the scratch length at four loading forces, F_N, of 500, 1000, 1500, and 2000 μN, are plotted in Fig. 4. The scratch depth as a function of the scratch length is also matched in Fig. 4 to reflect the profile of the scratching process. The unstable stage in the time range from 0 to 3 s is excluded. After the unstable stage, the lateral force eventually increases with the scratch length, which is attributed to the slightly increasing loading force programmed by the nanoindentation machine system parameter. It can also be seen that both the lateral force and the scratch depth randomly fluctuate with the scratch length, which is a so-called stick-slip behavior. The maximum undulation amplitudes of the lateral force at loading forces of 500, 1000, 1500, and 2000 μN are 11.49, 14.60, 17.90, and 18.75 μN, respectively. The maximum undulation amplitudes of the scratch depth at the above four loading forces are 7.13, 7.33, 7.99, and 8.02 nm, respectively. The morphologies of the

nanoscratches at different load forces have been inserted in Fig. 4. It can be seen that all the nanoscratches at different loading forces demonstrate a similar feature, namely a groove with some pileup of materials.

AFM observation is carried out to characterize the scratch-trace morphologies at different loading forces. The three-dimensional (3D) morphologies of the scratch traces at four loading forces are shown in Fig. 5(a). To quantitatively characterize the pileup of the materials around the groove, the profile of the section of the groove is plotted in Fig. 5(b). The profile of the section is along the yellow lines in Fig. 5(a), which is perpendicular to the scratching direction. The total depth between the groove and the pileup of the material around the groove are marked in Fig. 5(b). At a loading force of 500 μN, although the groove can be observed by SEM [Fig. 4(a)], the profile of the section does not show the significant groove and the pileup of the material around the groove [Fig. 5(b)]. With increasing loading force, the groove and the pileup of the material around the groove become more significant. The total height, which is the depth of the groove plus the pileup height, as a function of the loading force is plotted in Fig. 5(d). The total height at each loading force is averaged from five measurements. It can be seen that the total height changes linearly with loading force. The formation of pileup resulting from the plastic deformation underneath the nanoindentor tip also contributes to the stick-slip behavior. To further observe the shear separation of the glassy phase under the tip of the nanoindentor, the cross-section profile of the bottom of the grooves at different loading forces are plotted in Fig. 5(c). It can be seen that the profile undulation is also observed on the bottom of grooves. The undulation amplitudes of the bottom profiles at different loading forces were measured and are shown in Fig. 5(d). The undulation amplitude is approximately 15 nm at 500 μN. With increasing loading force, the amplitude slightly increases to approximately 22 nm at 2000 μN, although the value change is within the range of errors. The influence of the monocrystalline silicon substrate would be ruled out in the research, as the thickness of the $Ni_{62}Nb_{38}$ metallic glass film (2 μm) is almost 200 times thicker than the scratch depth (no more than 10 nm) [32].

The friction coefficient, μ, as a function of scratching time, t, is shown in Fig. 6. The enlarged curve of the friction coefficient versus scratching time is presented in the inset of Fig. 6, which presents $\Delta\mu$ and Δt in a serration event. The friction coefficient is a ratio of the lateral force and the loading force, which suggests that the fluctuation of the lateral force also corresponds to the change in the friction coefficient.

The SEM and AFM observations do not provide enough results to describe the fluctuation mechanism of the lateral force (or the scratch depth). Therefore, further exploration of the hidden information in the curves of the wavy lateral force (or the scratch depth) as a function of time (Fig. 7) is required. Enlarged curves of the lateral force versus time are shown in the inset of Fig. 7. It can be seen that the curve of the lateral force versus time is composed of numerous serration events, i.e., the stick-slip movements. Each serration event includes a force-increasing process and a force-decreasing process. During the force-increasing process, the structural strengthening in the atomic scale occurs, which facilitates accommodation of the plastic shear-strain. Once the force approaches the maximum value, i.e., the peak value, these clusters are activated to initiate the cooperative shearing that delivers the shear strain in the force-decreasing process. The force decrease corresponds to a force relaxation and usually causes a shear separation of the surface of metallic glasses, which results in some materials piling up around the grooves (Fig. 5) [33]. The average lateral force-increasing time, t_I, and the average relaxation time, t_R, are marked in the inset of Fig. 7. Table 1 shows that the ratio, R ($=t_I/t_R$), at loading forces of 500 and 2000 μN are 2.43 and 2.13, respectively, which are larger than those at 1000 μN (R=1.79) and 1500 μN (R=1.86).

To further characterize the stick-slip behavior in the lateral force, dynamic analysis is carried out. The differential lateral force, $|dF_L/dt|$, is plotted in the right-hand column of Fig. 7, which reflects the bursts of the shear-separation activity. The time interval between two neighboring serration events, t_n, is marked in the $|dF_L/dt|$-vs-t curves. It should be noted that the larger $|dF_L/dt|$ means a larger fluctuating amplitude of the lateral force rate, which reflects a more significant shear-separation activity in the stick-slip behavior. Thus, t_n is the time interval between two neighboring relatively larger serration events (see the Supplementary Material). At loading forces of 500 and 2000 μN, the bursts of the shear separation exhibit roughly the same periodicity between any two relatively larger neighboring serration events, which suggests that the t_n values are homogeneous (i.e., $t_{n-1}\approx t_n\approx t_{n+1}$). The t_n values are 1.09×10^{-1} and 3.58×10^{-3} s, respectively, at loading forces of 500 and 2000 μN. This homogeneous distribution of the time interval indicates a characteristic of chaotic behavior [34]. At loading forces of 1000 and 1500 μN, the time intervals (t_n) are inhomogeneous (i.e., $t_{n-1}\neq t_n\neq t_{n+1}$), which suggests that the serration events lack any typical

timescale. The phenomenon may reflect a characteristic of a critical state.

4. Dynamic analysis

To characterize the dynamic behavior during the nanoscratching process, the phase-space concept is introduced to accurately determine the dynamical system model [35]. The curves of lateral force versus time at four loading forces provide effective force-time sequences, $\{F_L(t_i), (i=1,2,\ldots,N)\}$, for the dynamic analysis. In these experimental lateral force-time sequences of metallic glasses, the mathematical description of the stick-slip dynamical system is unknown. Because the mathematical description of the unknown dynamical system has the equivalent geometrical characteristics of the reconstructed m-dimensional phase space (where m is an embedding dimension), the dynamics can be studied through the reconstruction of the phase space. In this case, a proxy of the observed state in the lateral force-time sequences will be found for the phase-space reconstruction [35].

In the present analysis, Cao's method is chosen to calculate the embedding dimension, m, that can avoid the influence of the noise on the lateral force [36] (see the Supplementary Material). Wolf's method, based on the evolution of the phase trajectory, is used to calculate the largest Lyapunov exponent [37,38] (see the Supplementary Material). The time delay, τ, which contributes to the least phase-space correlation, is determined by the mutual information method [39]. This process produces a reconstructed phase space spanned by a m-dimensional vector. The initial reference space point is determined to be $\{A(t_i)$: $F_L(t_i)$, $F_L(t_{i+\tau})$,$\cdots$,$F_L(t_{i+(m-1)\tau}$, $i=1,2,\ldots,[N-(m-1)\tau]\}$. The trajectory of the space point evolution is shown in Fig. 8. According to the Euclidean distance formula between two points, the distance between the initial phase point, $A(t_1)$, and the nearest adjacent point, $B(t_1)$, is marked as $L(t_1) = \overline{A(t_1)B(t_1)}$ (Fig. 8). Increasing the time to t_2 $(= t_1 + k\Delta t_1)$, $A(t_1)$ and $B(t_1)$ evolve to $A(t_2)$ and $B(t_2)$, respectively. Then, the distance between $A(t_2)$ and $B(t_2)$ is $l(t_2) = \overline{A(t_2)B(t_2)}$. In the time duration, $k\Delta t_1$, the exponential growth rate of a segment, σ_1, can be expressed as

$$\sigma_1 = \frac{1}{t_2 - t_1} \ln \frac{l(t_2)}{L(t_1)}. \quad (1)$$

The nearest adjacent point, $C(t_2)$, is shown in Fig. 8. The distance between $A(t_2)$ and $C(t_2)$ is $L(t_2) = \overline{A(t_2)C(t_2)}$. When the time evolves to t_3 $(= t_2 + k\Delta t_2)$, $A(t_2)$ and $C(t_2)$ change to $A(t_3)$ and $C(t_3)$, respectively. The distance between $A(t_3)$ and $C(t_3)$ is $l(t_3) = \overline{A(t_3)B(t_3)}$. Then, σ_1 becomes

σ_2, and the above procedure is repeated to the end of the point set. The total iteration steps and time are denoted M and t_M, respectively. The average exponential growth rate of M is calculated to be the largest Lyapunov exponent, λ_1,

$$\lambda_1 = \frac{1}{t_M - t_1} \sum_{i=2}^{M} \ln \frac{l(t_i)}{L(t_{i-1})}. \quad (2)$$

According to Eq. (2), the largest Lyapunov exponent can be evaluated, which quantitatively describes the converging or diverging of the phase-space adjacent track [40,41]. The largest Lyapunov exponent as a function of loading force is presented in Fig. 9. When the loading force is 500 μN, the largest Lyapunov exponent is 5.99×10^{-4}, which is a positive value. When the loading force increases from 1000 to 1500 μN, the largest Lyapunov exponent decreases from -3.44×10^{-4} to -8.80×10^{-4}, both of which are negative values. Increasing the loading force to 2000 μN results in the largest Lyapunov exponent being a positive value, 1.71×10^{-4}.

Detrended fluctuation analysis (DFA), based on the lateral force rate signal, $\left\{\frac{dF_L(t_i)}{dt}, i = 1,2,\ldots, N\right.$, is applied to explore the temporal-scaling behavior of nanoscratching. No-stationarities-like trends should be distinguished from the intrinsic fluctuations of the experimental data to find the correct scaling behavior of the fluctuations. DFA is a well-established method, specific to the analysis of time-series long-range correlation, for determining the scaling behavior of noisy data [42–44]. The time series of $\{x_{(i)}=dF_L(t_i)/dt, i=1,2,\ldots,N\}$ is divided into N_q (where $N_q=N/q$) zones, and the kth zone is defined as $x_k(j)$, $j=1,2,\ldots,q$. The local trend function, $\hat{x}_k(j)$, which is a linear function, is used to fit the q element of $x_k(j)$. A detrended time series is defined as $x_k(j) - \hat{x}_k(j), j = 1,2,\cdots,q$. Its mean-square error is $F^2(k) = \frac{1}{q}\sum_{j=1}^{q}(x_k(j) - \hat{x}_k(j))^2$. The root mean square of the total N_q zones, $F^2(k)$, is expressed as $F_q = (\frac{1}{N_q}\sum_{k=1}^{N_q} F^2(k))^{\frac{1}{2}}$. By altering the interval size, q, and repeating the above process, it can be deduced that F_q is a power function of the scale, q, $F_q: q^H$, where H is the Hurst exponent reflecting the long-range memory dependence of the signal. The H value as a function of loading force is plotted in Fig. 10. The H value at a loading force of 500 μN is 0.68, which is the minimum value among the four loading forces. When the loading force increases, the H value reaches a turning point of 0.75 at a loading force of 1000 μN.

The fractal dimension, D, is a sign of a local property. The box-counting method is used to calculate the D value [45]. Based on the lateral force-rate signal, $\frac{dF_l(t_i)}{dt}, i = 1,2,\cdots N,$ the square

boxes, $N(l)$, with a length, l, cover the total dataset. A series of $N(l)$ are obtained by changing the box size of l. Fitting $[l,N(l)]$ in a double-logarithmic plot, the slope of the fitting curve is expressed as $D = -\lim_{l\to 0} \frac{\ln N(l)}{\ln l}$. The D value as a function of loading force is plotted in Fig. 10. When the loading force is 500 μN, the D value of 1.32 is the maximum one among the values of the four loading forces. Upon increasing the loading force to 2000 μN, the D value slightly decreases to 1.26.

5. Discussion

5.1 Shear-branching process in nanoscratching

Owing to the unrelaxed state in the current metallic glass film, some heterogeneous structures, such as free volumes [46,47], shear transformation zones (STZs) [48,49], etc., exist. The local properties of the heterogeneous structure, and the specifically local atomic arrangements give rise to clusters with a lower shear modulus [13,14]. These are expected to mediate plastic flow at the scale of the shear deformation, or can merge into shear bands. The increase of loading force leads to the augmentation of the contact area between the nanoindentor and the metallic glass film, resulting in an increase of the friction force that improves the lateral force during scratching. In this case, the quantity of the locally heterogeneous structures in metallic glasses is improved [50]. These heterogeneous structures possess lower strength and high atomic liquidity, i.e., lower shear modulus, and are at a higher-energy state [51,52]. Once the tip of the nanoindentor contacts the surface of metallic glasses, a large quantity of clusters with low shear modulus causes the nanoscratching process to be unstable, resulting in large fluctuations in lateral force and depth at a high loading force, as shown in Fig. 4.

Based on Figs. 4 and 5, it is clear that the undulation amplitude measured from the nanoindentation instrument is always smaller than the value measured from the AFM images. The profile of the cross-section of the bottom of the groove actually reflects the morphology of the elastic recovered glassy phase after the tip of the nanoindentor has cut through the surface. The nanoscratching process is illustrated in Fig. 11. It can be seen that the nanoindentor scratching on the surface of the film can generate a depth, d_p. After that, the elastic recovery induced by the indentation action of the scratching process can cause a recovery depth, d_{er}. In this case, the recovery depth can contribute to the depth undulation, which is the possible reason that the depth

undulation measured from the AFM image is larger than that from the nanoindentation instrument. The recovered depth is only several nanometers in the current study. The fluctuation of the scratch depth ranged from 15 to 22 nm based on the AFM images, which is comparable to the typical size of a shear band. Numerous shear-branching processes are conjectured to have been activated. In this case, the depth undulation should be linked to the relaxation behavior, static aging, and the stick-slip behavior [20]. Recent research also found that the nanosized surface layer (with a size of approximately 20 nm) of metallic glasses undergoes characteristically structural evolutions, including stochastically structural rearrangement, local relaxation, and rejuvenation [53]. As such, shear branching occurs underneath the tip of the nanoindentor.

During the nanoscratching process, the tip of the nanoindentor cutting through the surface of sample causes the formation of sideways-flowing materials that pile up around two sides of the nanoscratch (Fig. 5). In front of the tip, the materials accumulate but are not removed, playing an important role in the stick-slip movement of the nanoindentor [54,55]. During the sideways-flowing process, parallel shear bands at the edge of the scratching tracks after nanoscratching should usually be formed [56]. Thus, shear branching is the main mechanism dominating the scratching process of the nanoindentor, which forms a shear-band-structure-like state.

As demonstrated by Eq. (2), when the largest Lyapunov exponent is positive, the phase-space adjacent track is diverging, and the motion is chaotic. When the largest Lyapunov exponent is negative, the phase-space adjacent track is convergent, i.e., a stable motion [57,58]. At loading forces of 500 and 2000 μN, the time intervals marked in Figs. 7(b) and 7(h) are homogeneous, showing typically periodic timescales. This phenomenon suggests a characteristic of chaotic behavior, which is verified by the positive largest Lyapunov exponent. The R ($=t_I/t_R$) values are higher than 2 at loading forces of 500 and 2000 μN, which means that the force accumulation time, t_I, is much larger than the force relaxation time, t_R. In this case, the accumulated force is quickly relaxed in each serration event, and there is almost no interference between neighboring serration events in the temporal space. This contributes to form the characteristic of chaotic behavior. The time intervals marked in Figs. 7(d) and 7(f) are inhomogeneous, suggesting that the serration events lack any typical timescale when the loading force is in the range 1000–1500 μN. In this loading-force range, smaller R values, as compared to the values at loading forces of 500 and 2000 μN, suggest that the force relaxation time is relatively longer in a serration event. Thus, the accumulated force in serration events cannot be fully relaxed during a limited time, which enhances

the temporal correlation between neighboring serration events, and leads to the inhomogeneous time interval. This is a characteristic of convergent adjacent serrations, which indicates a stable motion.

5.2 Fractal dimension in nanoscratching

The fractal dimension, *D*, describes the complexity of a system, which is a sign of the local properties of the lateral force fluctuation and of the shear-branching process. A larger *D* value means that the system is more complex. Nanoscratching is actually an interaction process between the nanoindentor and the atoms on the surface of the metallic glass film. Regarding the occurrence of the shear-branching process [59–65], this interaction includes two kinds of processes, i.e., the adsorption of the atoms on the nanoindentor tip, and the flow units activated [66]. When the loading force is small, e.g., 500 μN, a few atoms on the surface can adsorb onto the nanoindentor tip due to the interactions of the van der Waals attractive force between the surface and the nanoindentor tip [66]. Since the loading force is small, the depth of the nanoscratch is not significant, which is confirmed by the AFM results (Fig. 5). A slight extent of deformation then occurs on the surface caused by the interactions of repulsive forces. The removed atoms do not significantly pile up around the groove. Increasing the loading force causes the amount of deformation on the surface underneath the nanoindentor tip to gradually increase with increasing indentation depth. The removed atoms are pushed and moved along the edges of the nanoindentor tip, with a few underneath the nanoindentor tip being moved downward. Thus, a great number of clusters with low shear modulus independently develop in the contact area between the nanoindentor tip and the surface, which are the fundamental units of shear deformation in metallic glasses. As such, at a higher loading force, the motion of lateral force corresponds to the operation of shear branching during the nanoscratching process, which is a relatively simple mechanism. At a smaller loading force, the adsorption of the surface atoms on the nanoindentor tip brings out some forces that influence the lateral force. Therefore, the local properties of the lateral force at a smaller loading force are more complex than those at a higher loading force, which is manifested by a larger *D* value.

5.3 Detrended fluctuation analysis

The Hurst exponent, *H*, is a sign of the global property of the shear-branching structure. The local property reflected in the global one is revealed by a self-affine model [67], i.e.,

$$D+H=n+1, \tag{3}$$

where n is the spatial dimension. The modified Cauchy class combines the Hurst exponent and the fractal dimension, with a correlation function of a Gaussian random processes, and an isotropic random field in R^n, as shown in [68],

$$C(h) = (1 + |h|^{\alpha})^{-\frac{\beta}{\alpha}-1}[1 + (1-\beta)|h|^{\alpha}] \quad h \in R^n, \tag{4}$$

where $\alpha \in (0,2]$, $\beta > 0$, and we have

$$H = 1 - \beta/2. \tag{5}$$

When $H \in (0.5,1)$, a restriction of $\beta \in (0,1)$ is obtained from Eq. (5). Then, a positive correlation of the signal is obtained from Eq. (4). In this case, the evolution of shear branching is consistent with the past state for the long-memory dependency. It suggests that the shear-branching process is a persistent process when the loading force ranges from 500 to 2000 μN. With increasing loading force, the Hurst exponent increases to the maximum value of 0.75 at 1000 μN, and then decreases. The loading force of 1000 μN can be viewed as a critical point. For β=1, Eq. (4) shows that the time series evolves in the manner of a memoryless random walk, which results in a homogeneous process to some extent. At the same time, H=0.5 is obtained from Eq. (5). When the H value is far from 0.5, the shear-branching process evolves inhomogeneously. Thus, the maximum H value at the critical point of 1000 μN suggests that shear branching is the most inhomogeneous process. The inhomogeneous shear-branching process leads to an inhomogeneous stick-slip event, contributing to the inhomogeneous lateral force rate signals. The conclusion is consistent with the analysis that the R ratio is the smallest (1.79) at 1000 μN in Table 1, meaning a relatively long relaxation time for stick-slip events. This suggests that a temporal correlation between neighboring stick-slip events is the strongest at a loading force of 1000 μN. On the other hand, the smaller H value, at loading forces of 500 and 2000 μN, suggests a more homogeneous shear-branching process compared to those at the loading forces of 1000 and 1500 μN, i.e., the larger H value. The decreased interaction between the neighboring stick-slip events causes a high degree of homogeneous stick-slip events. This is in agreement with the positive largest Lyapunov exponent, which is characterized by the chaotic behavior. In addition, an inner correlation between H and D is described by Eq. (3). In our experiment, the nanoscratching is regarded as a line that is one dimensional in space. Thus, the n value in Eq. (3) is taken as 1. Thus, D+H=2, which suggests a self-similar random process. The sum of D and H, calculated from the experiment, is close to 2 at different loading forces. This shows that the lateral force rate signal is close to a self-similar random

process, when the loading force ranges from 500 to 2000 μN.

5.4 Confidential interval analysis

The characteristics of the shear-branching process, such as complexity and homogeneity, must be manifested in the changes in the friction coefficients. The inhomogeneous shear-branching process leads to an inhomogeneous stick-slip event, which could contribute to the inhomogeneous lateral force rate signals. In this case, the differential friction coefficient, i.e., $d\mu/dt$, can be used to reflect the stability of the stick-slip process. The values of $d\mu/dt$ at different loading forces as a function of time at various loading forces are plotted in Figs. 12(a), 12 (c), 12(e), and 12(g). It can be seen that most of values of $d\mu/dt$ at each loading force fluctuate around zero value, and are distributed within a wide zone. To quantitatively describe the distribution of these values of $d\mu/dt$, a statistical analysis is carried out. The histogram of $d\mu/dt$ versus relative frequency is presented in Figs. 12(b), 12(d), 12(f), and 12(h). Gaussian fitting is used to profile the histogram, which provides the average value, $\bar{\mu}$, and the standard deviation, σ, of the values of $d\mu/dt$. A confidence interval is introduced to characterize the distribution zone of the values of $d\mu/dt$. In the present study, a 99% confidence interval, which means that 99% of the values of $d\mu/dt$ are included in this zone, is chosen as the distribution zone in the $d\mu/dt$-versus-time curve. The calculation of the boundaries of the distribution zone is [69]

$$C_1=\bar{\mu}-2.576\sigma, \quad (6)$$

$$C_2=\bar{\mu}+2.576\sigma, \quad (7)$$

where C_1 is the 99% confidence lower limit and C_2 the 99% confidence upper limit. According to the values of $\bar{\mu}$ and σ listed in Fig. 12, the confidence intervals $[C_1,C_2]$ at loading forces of 500, 1000, 1500, and 2000 μN are calculated to be [−0.48,0.61], [−0.21,0.26], [−0.14,0.17], and [−0.12,0.14], respectively, which are indicated by the dashed lines in Figs. 12(a), 12(c), 12(e), and 12(g). It is obvious that the confidential interval at 500 and 1000 μN is large in the cases of the four loading forces. With increasing loading force, the size of the confidence interval decreases. A larger confidence interval indicates a larger fluctuation range of the value of $d\mu/dt$, which means that the shear-branching process trends to be more complex. The complexity of the shear-branching process decreases with increasing loading force, which is verified by the decreasing fractal dimension as well.

Although above statistical analysis determines the confidential intervals at the four loading forces, the experimental results show that in addition to the values of $d\mu/dt$ covered in the

confidence interval, some values of $d\mu/dt$ are scattered outside the confidence interval, which reflects the inhomogeneous shear-branching process. Therefore, the percentages of the values located outside the confidence interval are calculated as 3.80% (500 μN), 6.50% (1000 μN), 6.41% (1500 μN), and 6.19% (2000 μN). It is clear that the nanoscratching process at a loading force of 500 μN has the lowest value, which suggests that the case at 500 μN is the most homogeneous for the four loading forces. On the other hand, the nanoscratching process at a loading force of 1000 μN has the highest value, which suggests that the case at 1000 μN is the most inhomogeneous for the four loading forces. The inhomogeneous shear-branching process in the nanoscratching process at a loading force of 1000 μN is consistent with the maximum Lyapunov exponent and the Hurst exponent. The above statistical analysis illuminates that at a constant scratching speed the loading force should be an optimal value, which can influence the roughness of the machined surface, especially the on the nanoscale or during ultraprecise machining.

The above-described analysis method originates from nonlinear dynamic theory, which is a universal mathematical theory. It has been widely applied in such cross-disciplinary fields as financial mathematics and biomathematics. It can be applied in different materials, for example, a polycrystalline metal. The results depend on the structure and some intrinsic properties of the polycrystalline metal. Our study links the deformation characteristics of the metallic glass to the dynamics of the stick-slip behavior. It provides a new dynamic viewpoint for researching the nanoscratching process and is helpful for understanding the chaotic and the critical state of nanoscratching from the perspective of force relaxation. However, for a polycrystalline metal, when the nanoindentor tip cuts through the surface, the deformation of the grains underneath the tip is dominated by the operation of the crystallographic defects, such as the activation of dislocations. In this case, the dynamics of the stick-slip behavior during the nanoscratching process may be different than in metallic glasses.

6. Conclusions

The stick-slip dynamics of nanoscratching on $Ni_{62}Nb_{38}$ metallic glass film was investigated. Based on the lateral-force–versus–time curves and on the friction coefficient, the complexity in temporal-spatial space of the shear-branching process during nanoscratching experiments was studied at different loading forces. The shear-branching process during the nanoscratching process was found to be stochastic. With increasing loading force, a transition between chaotic and stable

states of the stick-slip dynamics was observed. The adsorption of the surface atoms on the nanoindentor tip and the flow units' activation was found to have a significant influence on the fractal dimension of the lateral force. Detrended fluctuation analysis found a positive correlation process during the shear-branching process. At a critical loading force of 1000 μN, the Hurst exponent reached the maximum value, implying that there is inhomogeneity in the shear-branching process. The value of $D+H$ was closest to 2, suggesting that the shear-branching process is close to a self-similar random process when loading force ranges from 500 to 2000 μN.

Acknowledgements

The authors would like to acknowledge the financial support from the National Key Basic Research Program from MOST (No. 2015CB856800), the NSFC (Grant Nos. 11271339, 51671120, and 51501106), the 111 project, the Plan for Scientific Innovation Talent of Henan Province (164200510011), and Innovative Research Team of Science and Technology in Henan Province (17IRTSTHN007). PKL thanks the U.S. National Science Foundation (DMR-1611180) with the program director of Dr. Farkas, the Department of Energy, National Energy Technology Laboratory (DE-FE-0011194 and DE-FE-0024054) with the program management of Dr. J. Mullen and Mr. R. Dunst and the U.S. Army Research Office (W911VF-13-1-0438) with the program director of Dr. D. M. Stepp.

References

[1] A.D. Moghadam, E. Omrani, P.L. Menezes, P.K. Rohatgi, Mechanical and tribological properties of self-lubricating metal matrix nanocomposites reinforced by carbon nanotubes (CNTs) and graphene-a review, Compos. Part B-Eng. 77 (2015) 402-420.

[2] D. Kawashima, Y. Asako, Data reduction of friction factor of compressible flow in micro-channels, Int. J. Heat Mass. Tran. 77 (2014) 257-261.

[3] T. Junge, J.F. Molinari, Plastic activity in nanoscratch molecular dynamics simulations of pure aluminium, Int. J. Plasticity 53 (2014) 90-106.

[4] D.X. Han, G. Wang, J. Li, K.C. Chan, S. To, F.F. Wu, Y.L. Gao, Q.J. Zhai, Cutting characteristics of Zr-based bulk metallic glass, J. Mater. Sci. Technol. 31 (2015) 153-158.

[5] E.A. Jagla, F.P. Landes, A. Rosso, Viscoelastic effects in avalanche dynamics: A key to earthquake statistics, Phys. Rev. Lett. 112 (2014) 174301.

[6] W.M. Ke, F.C. Zhang, Z.N. Yang, M. Zhang, Micro-characterization of macro-sliding wear for steel, Mater. Charact. 82 (2013) 120-129.

[7] P. Qing, S.B. Huang, S.S. Gao, L.M. Qian, H.Y. Yu, Effect of gamma irradiation on the wear behaviour of human tooth enamel, Sci. Rep. 5 (2015) 11568.

[8] A. Dasari, Z.Z. Yu, Y. W. Mai, Nanoscratching of nylon 66-based ternary nanocomposites, Acta Mater. 55 (2007) 635-646.

[9] T. Bohlein, J. Mikhael, C. Bechinger, Observation of kinks and antikinks in colloidal monolayers driven across ordered surfaces, Nat. Mater. 11 (2012) 126-130.

[10] W. Chen, A.S. Foster, M.J. Alava, L. Laurson, Stick-slip control in nanoscale boundary lubrication by surface wettability, Phys. Rev. Lett. 114 (2015) 095502.

[11] X.Z. Liu, Z.J. Ye, Y.L. Dong, P. Egberts, R.W. Carpick, A. Martini, Dynamics of atomic stick-slip friction examined with atomic force microscopy and atomistic simulations at overlapping speeds, Phys. Rev. Lett. 114 (2015) 146102.

[12] Y.H. Liu, G. Wang, R.J. Wang, D.Q. Zhao, M.X. Pan, W.H. Wang, Super plastic bulk metallic glasses at room temperature, Science 315 (2007) 1385-1388.

[13] C.J. Byrne, M. Eldrup, Bulk metallic glasses, Science 321 (2008) 502-503.

[14] Z.Q. Liu, L. Huang, W. Wu, X.K. Luo, M.J. Shi, P.K. Liaw, W. He, T. Zhang, Novel low Cu content and Ni-free Zr-based bulk metallic glasses for biomedical applications, J. Non-Cryst. Solids 363 (2013) 1-5.

[15] L. Huang, Y. Yokoyama, W. Wu, P.K. Liaw, S.J. Pang, A. Inoue, T. Zhang, W. He, Ni-free Zr-Cu-Al-Nb-Pd bulk metallic glasses with different Zr/Cu ratios for biomedical applications, J. Biomed. Mater. Res. B 100 (2012) 1472-1482.

[16] A. Wiest, G.Y. Wang, L. Huang, S. Robert, M.D. Demetrious, P.K. Liaw, W.L. William, Corrosion and corrosion fatigue of vitreloy glasses containing low fractions of late transition metals, Scripta Mater. 62 (2010) 540-543.

[17] L. Huang, D.C. Qiao, B.A. Green, P.K. Liaw, J.F. Wang, S.J. Pang, T. Zhang, Bio-corrosion study on zirconium-based bulk-metallic glasses, Intermetallics 17 (2009) 195-199.

[18] L. Xia, S.T. Shan, D. Ding, Binary bulk metallic glass $Ni_{62}Nb_{38}$ with high compressive strength of 3100MPa, Intermetallics 15 (2007) 1046-1049.

[19] E. Brinksmeier, R. Gläbe, L. Schönemann, Review on diamond-machining processes for the generation of functional surface structures, CIRP-J Manuf. Sci. Technol. 5 (2012) 1-7.

[20] R. Maaß, J.F. Löffler, Shear-band dynamics in metallic glasses, Adv. Funct. Mater. 25 (2015) 2353-2368.

[21] H.B. Ke, B.A. Sun, C.T. Liu, Y. Yang, Effect of size and base-element on the jerky flow dynamics in metallic glass, Acta Mater. 63 (2014) 180-190.

[22] B.A. Sun, W.H. Wang, The fracture of bulk metallic glasses, Prog. Mater. Sci. 74 (2015) 211-307.

[23] J.L. Ren, C. Chen, Z.Y. Liu, R. Li, G. Wang, Plastic dynamics transition between chaotic and self-organized critical states in a glassy metal via a multifractal intermediate, Phys. Rev. B 86 (2012) 134303.

[24] J.O. Krisponeit, S. Pitikaris, K.E. Avila,S. Küchemann, A. Krüger, K. Samwer, Crossover from random three-dimensional avalanches to correlated nano shear bands in metallic glasses, Nat. Commun. 5 (2014) 3616.

[25] S.Y. Chen, L.P. Yu, J.L. Ren, X. Xie, X.P. Li, Y. Xu, G.F. Zhao, P.Z. Li, F.Q. Yang, Y. Ren, P.K. Liaw, Self-similar random process and chaotic behavior in serrated flow of high entropy alloys, Sci. Rep. 6 (2016) 29798.

[26] J.L. Ren, C. Chen, G. Wang, W.S. Cheung, B.A. Sun, N. Mattern, S. Siegmund, J. Eckert, Various sizes of sliding event bursts in the plastic flow of metallic glasses based on a spatiotemporal dynamic model, J. Appl. Phys. 116 (2014) 033520.

[27] J.L. Ren, C. Chen, G. Wang, N. Mattern, J. Eckert, Dynamics of serrated flow in a bulk metallic glass, AIP Adv. 1 (2011) 032158.

[28] X.L. Bian, G. Wang, H.C. Chen, L. Yan, J.G. Wang, Q. Wang, P.F. Hu, J.L. Ren, K.C. Chan, N. Zheng, A. Teresiak, Y.L. Gao, Q.J. Zhai, J. Eckert，J. Beadsworth, K.A. Dahmen, P.K. Liaw, Manipulation of free volumes in a metallic glass through Xe-ion irradiation, Acta Mater. 106 (2016) 66-77.

[29] G. Sparks, P.S. Phani, U. Hangen, R. Maaβ, Spatiotemporal slip dynamics during deformation of gold micro-crystal, Acta Mater. 122 (2017) 109-119.

[30] R.D. Marco, Z.T. Jiang, B. Pejcic, A.Y. Riessen, In situ synchrotron radiation grazing incidence X-ray diffraction-A powerful technique for the characterization of solid-state ion-selective electrode surfaces, Electrochim. Acta 51 (2006) 4886-4891.

[31] S. Kawana, M. Durrell, J. Lu, J.E. Macdonald, M. Grell, D.D.C. Bradley, P.C. Jukes, R.A.L. Jones, S.L. Bennett, X-ray diffraction study of the structure of thin polyfluorene films, Polymer

43 (2002) 1907-1913.

[32] A.C. Fischer-Cripps, Contact mechanics, Springer, New York, 2011.

[33] M. Bakkal, A.J. Shih, R.O. Scattergood, C.T. Liu, Machining of a Zr-Ti-Al-Cu-Ni metallic glass, Scripta Mater. 50 (2004) 583-588.

[34] M. Koslowski, R. LeSar, R. Thomson, Avalanches and scaling in plastic deformation, Phys. Rev. Lett. 93 (2004) 125502.

[35] S.H. Strogatz, Nonlinear dynamics and chaos: with applications to physics, biology, chemistry, and engineering, Westview press, Philadelphia, 2014.

[36] L.P. Cao, Practical method for determining the minimum embedding dimension of a scalar time series, Physica D 110 (1997) 43-50.

[37] A. Wolf, J.B. Swift, H.L. Swinney, J.A. Vastano, Determining Lyapunov exponents from a time series, Physica D16 (1985) 285-317.

[38] S. Sato, M. Sano, Y. Sawada, Practical methods of measuring the generalized dimension and the largest Lyapunov exponent in high dimensional chaotic systems, Prog. Theo. Phys. 77 (1987) 1-5.

[39] A.M. Fraser, H.L. Swinney, Independent coordinates for strange attractors from mutual information, Phys. Rev. A 33 (1986) 1134.

[40] M.T. Rosenstein, J.J. Collins, C.J. De Luca, A practical method for calculating largest Lyapunov exponents from small data sets, Physica D 65 (1993) 117-134.

[41] E.S. Key, Lower bounds for the maximal Lyapunov exponent, J. Theor. Probab. 3 (1990) 477-488.

[42] M.S. Movahed, G.R. Jafari, F. Ghasemi, S. Rahvar, M.R.R. Tabar, Multifractal detrended fluctuation analysis of sunspot time series, J. Stat. Mech. 2006 (2006) P02003.

[43] C. Matsoukas, S. Islam, I. Rodriguez-Iturbe, Detrended fluctuation analysis of rainfall and streamflow time series, J. Geophys. Res. 105 (2000) 29165-29172.

[44] C. Chen, J.L. Ren, G. Wang, K.A. Dahmen, P.K. Liaw, Scaling behavior and complexity of plastic deformation for a bulk metallic glass at cryogenic temperatures, Phys. Rev. E 92 (2015) 012113.

[45] T. Vicsek, Fractal Growth Phenomena, World Scientific, Singapore, 1992.

[46] F. Spaepen, A microscopic mechanism for steady state inhomogeneous flow in metallic glasses, Acta metal. 25 (1977) 407-415.

[47] F. Spaepen, Homogeneous flow of metallic glasses: A free volume perspective, Scripta mater. 54 (2006) 363-367.

[48] A.S. Argon, Plastic deformation in metallic glasses, Acta metal. 27 (1979) 47-58.

[49] A.S. Argon, H.Y. Kuo, Plastic flow in a disordered bubble raft (an analog of a metallic glass), Mater. Sci. Eng. (39) 1979 101-109.

[50] H.L. Peng, M.Z. Li, W.H. Wang, Structural signature of plastic deformation in metallic glasses, Phys. Rev. Lett. 106 (2011) 135503.

[51] L.S. Huo, J.F. Zeng, W.H. Wang, C.T. Liu, Y. Yang, The dependence of shear modulus on dynamic relaxation and evolution of local structural heterogeneity in a metallic glass, Acta Mater. 61 (2013) 4329-4338.

[52] Z. Wang, P. Wen, L.S. Huo, H.Y. Bai, W.H. Wang, Signature of viscous flow units in apparent elastic regime of metallic glasses, Appl. Phys. Lett. 101 (2012) 121906.

[53] Y.M. Lu, J.F. Zeng, J.C. Huang, S.Y. Kuan, T.G. Nieh, W.H. Wang, M.X. Pan, C.T. Liu, Y. Yang, In-situ atomic force microscopy observation revealing gel-like plasticity on a metallic glass surface, J. Appl. Phys. 121 (2017) 095304.

[54] D. Klaumünzer, R. Maaß, J.F. Löffler, Stick-slip dynamics and recent insights into shear banding in metallic glasses, J. Mater. Res 26 (2011) 1453-1463.

[55] G.N. Nielson, Scale effects in microindentation of ductile crystals, Massachusetts Institute of Technology, 1 (2000), 19-20.

[56] Y.J. Huang, Y.L. Chiu, J. Shen, Y. Sun, J.J.J. Chen, Mechanical performance of metallic glasses during nanoscratch tests, Intermetallics 18 (2010) 1056-1061.

[57] T. Richeton, J. Weiss, F. Louchet, Breakdown of avalanche critical behaviour in polycrystalline plasticity, Nat. Mater. 4 (2005) 465-469.

[58] M.C. Miguel, A. Vespignani, S. Zapperi, J. Weiss, J.R. Grasso, Intermittent dislocation flow in viscoplastic deformation, Nature 410 (2001) 667-671.

[59] R. Maaβ, P. Birckigt, C. Borchers, C.A. Volkert, Long range stress fields and cavitation along a shear band in a metallic glass: The local origin of fracture, Acta Mater. 98 (2015) 94-102.

[60] X. Tong, G. Wang, J. Yi, J.L. Ren, S. Pauly, Y.L. Gao, Q.J. Zhai, N. Mattern, K.A. Dahmen, P.K. Liaw, J. Eckert, Shear avalanches in plastic deformation of a metallic glass composite, Int. J. Plasticity 77 (2016) 141-155.

[61] D. Tönnies, R. Maaβ, C.A. Volkert, Room temperature homogeneous ductility of micrometer-

sized metallic glass, Adv. Mater. 26 (2014) 5715-5721.

[62] P. Thurnheer, R. Maaβ, K.J. Laws, S. Pogatscher, J.F. Löffler, Dynamic properties of major shear bands in Zr-Cu-Al bulk metallic glasses, Acta Mater. 96 (2015) 428-436.

[63] R. Maaβ, D. Klaumünzer, J.F. Löffler, Propagation dynamics of individual shear bands during inhomogeneous flow in a Zr-based bulk metallic glass, Acta Mater. 59 (2011) 3205-3213.

[64] C.T. Pan, T.T. Wu, C.F. Liu, C.Y. Su, W.J. Wang, J.C. Huang, Study of scratching Mg-based BMG using nanoindenter with Berkovich probe, Mater. Sci. Eng. A 527 (2010) 2342-2349.

[65] G. Wang, K.C. Chan, L. Xia, P. Yu, J. Shen, W.H. Wang, Self-organized intermittent plastic flow in bulk metallic glasses, Acta Mater. 57 (2009) 6146-6155.

[66] C.D. Wu, Molecular dynamics simulation of nanotribology properties of CuZr metallic glasses, Appl. Phys. A 122 (2016) 486.

[67] A. Malinverno, A simple method to estimate the fractal dimension of a self-affine series, Geophys. Res. Lett. 17 (1990) 1953-1956.

[68] T. Gneiting, M. Schlather, Stochastic models that separate fractal dimension and the Hurst effect, SIAM Rev. 46 (2004) 269-282.

[69] W. Liu, T. Miwa, A.J. Hayter, Simultaneous confidence interval estimation for successive comparisons of ordered treatment effects, J. Stat. Plan. Inter. 88 (2000) 75-86.

Table 1 Average lateral force-increasing time, t_I, average lateral force-decreasing time, t_R, $R=t_I/t_R$, time delay, τ, of the stick-slip sequence, embedding dimension, m, the largest Lyapunov exponent, λ_1, fractal dimension, D, Hurst index, H, and $D+H$, all at different loading forces.

Normal force (μN)	500	1000	1500	2000
t_I (s)	0.068±0.003	0.050±0.004	0.078±0.002	0.211±0.013
t_R (s)	0.028±0.003	0.028±0.003	0.042±0.003	0.099±0.004
R	2.43	1.79	1.86	2.13
τ	49	49	48	48
m	7	8	8	7
λ	5.99×10^{-4}	-3.44×10^{-4}	-8.80×10^{-4}	1.71×10^{-4}
D	1.317±0.006	1.282±0.007	1.273±0.0039	1.262±0.054
H	0.684±0.062	0.750±0.057	0.747±0.047	0.714±0.047
$D + H$	2.001±0.055	2.032±0.063	2.020±0.038	1.977±0.026

Figure captions

Fig. 1 GIXRD pattern of $Ni_{62}Nb_{38}$ metallic glass film.

Fig. 2 Determination of background noise. (a) Lateral force fluctuation during the air-scratching process. (b) Amplitude fluctuation of lateral force.

Fig. 3 Representative profile of nanoscratching process. Inset shows the enlarged curves corresponding to the region covered by dashed line.

Fig. 4 Lateral force and scratch depth as a function of scratch length. Insets show the corresponding nanoscratch morphology. (a), (b), (c), and (d) correspond to loading forces of 500, 1000, 1500, and 2000 μN, respectively.

Fig. 5 Morphology of the scratch traces observed by AFM. (a) 3D morphologies of the scratch traces at four loading forces. (b) Profile of the cross-section along the yellow lines in (a). (c) Profile of the cross-section along the blue dashed line in (a). (d) Height and amplitude as functions of loading force.

Fig. 6 Friction coefficient as a function of time. Inset shows the enlarged friction-coefficient–vs–time curve.

Fig. 7 Lateral force as a function of time. (a), (c), (e), and (g) show plots of lateral forces vs time at loading forces of 500, 1000, 1500, and 2000 μN, respectively. Insets show the enlarged lateral-force–vs–time curves. (b), (d), (f), and (h) present partial curves of $\left|\frac{dF_L}{dt}\right|$ vs time at loading forces of 500, 1000, 1500, and 2000 μN.

Fig. 8 Evolution of the phase-space trajectory.

Fig. 9 Largest Lyapunov exponent as a function of loading force.

Fig. 10 Hurst exponent, H, fractal dimension, D, and $D+H$ of $Ni_{62}Nb_{38}$ metallic glass film at loading forces of 500, 1000, 1500, and 2000 μN.

Fig. 11 Nanoscratching process. d_s is the scratch depth, d_{er} the elastic recover depth, α the angle of conic indentor [$\alpha=(\pi/3)$], Δl the unit scratch length, and d_p the penetration depth.

Fig. 12 Left-hand column, curves of differential friction coefficient vs time at different loading forces; right-hand column, curves of probability histogram of differential friction coefficient at different loading forces.

Figure(s)
Click here to download high resolution image

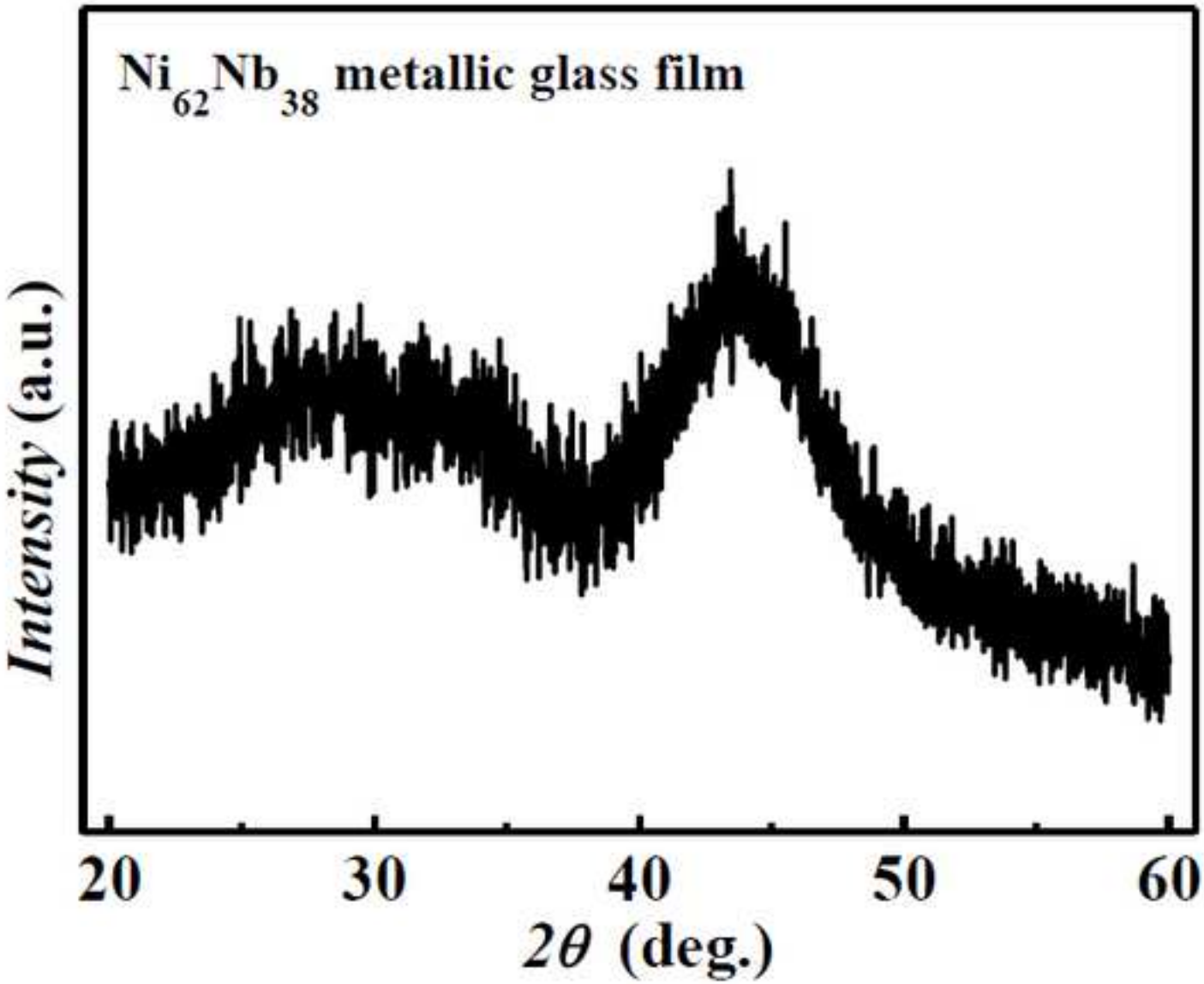

Fig. 1 GIXRD pattern of $Ni_{62}Nb_{38}$ metallic glass film.

Figure(s)
Click here to download high resolution image

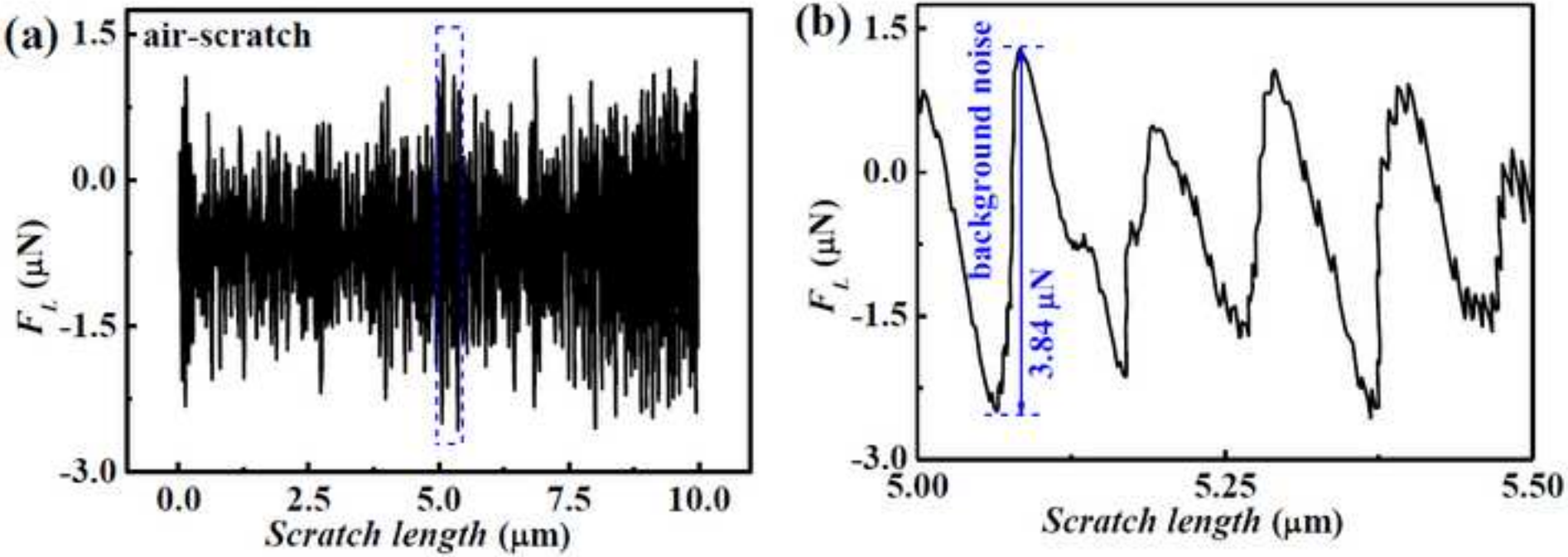

Fig. 2 Determination of background noise. (a) Lateral force fluctuation during the air-scratching process. (b) Amplitude fluctuation of lateral force.

Figure(s)
Click here to download high resolution image

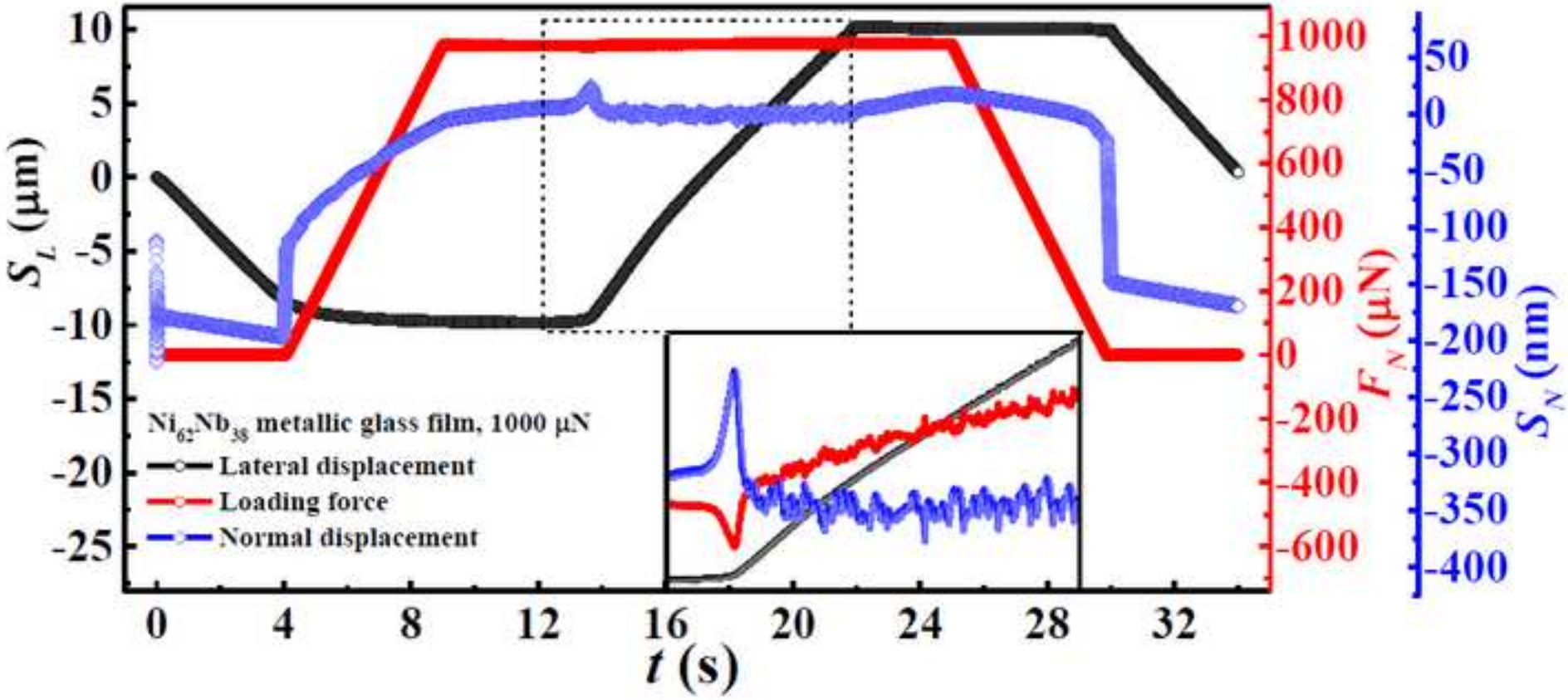

Fig. 3 Representative profile of nanoscratching process. Inset shows the enlarged curves corresponding to the region covered by dashed line.

Figure(s)

Click here to download high resolution image

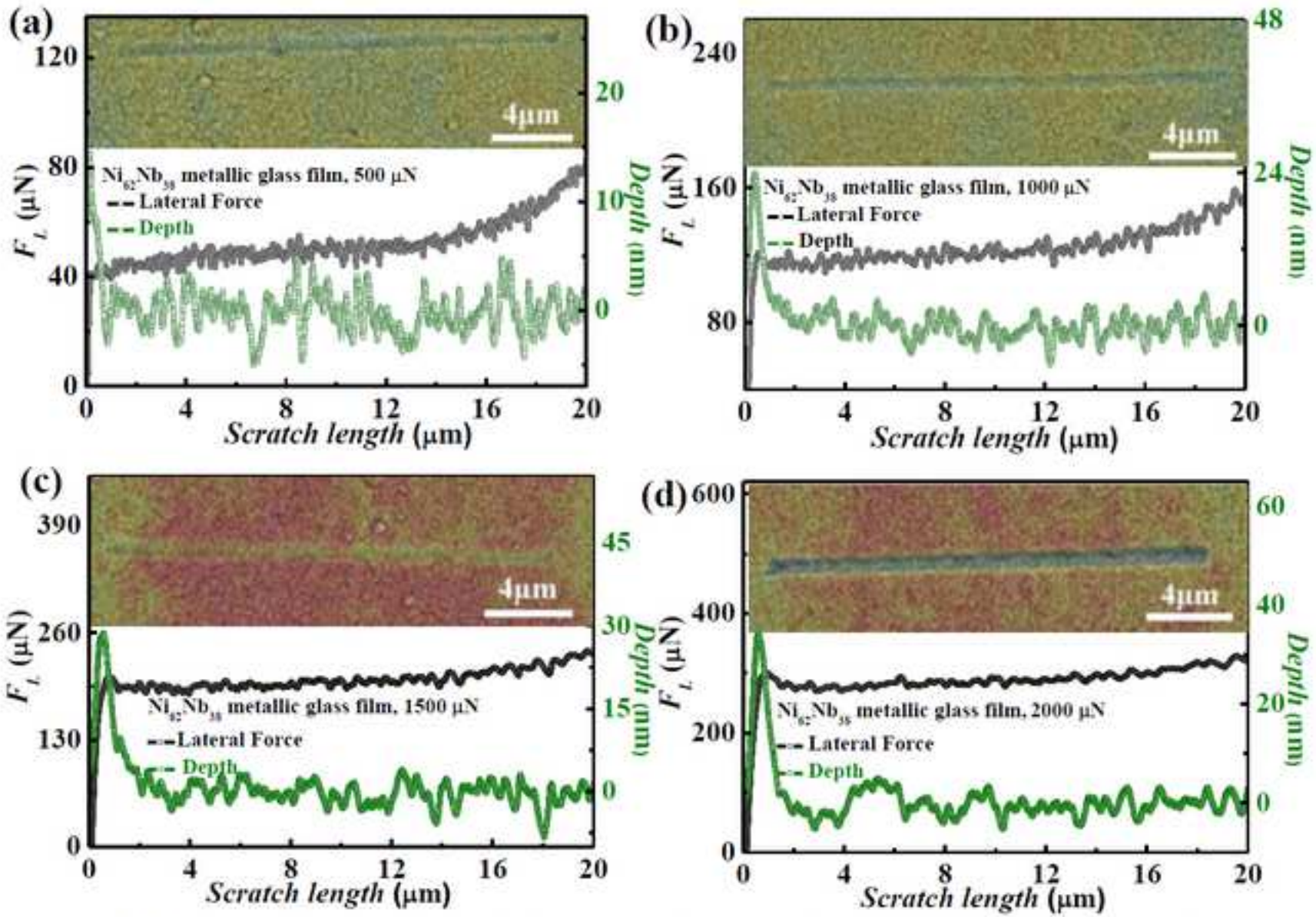

Fig. 4 Lateral force and scratch depth as a function of scratch length. Insets show the corresponding nanoscratch morphology. (a), (b), (c), and (d) correspond to loading forces of 500, 1000, 1500, and 2000 μN, respectively.

Figure(s)

Click here to download high resolution image

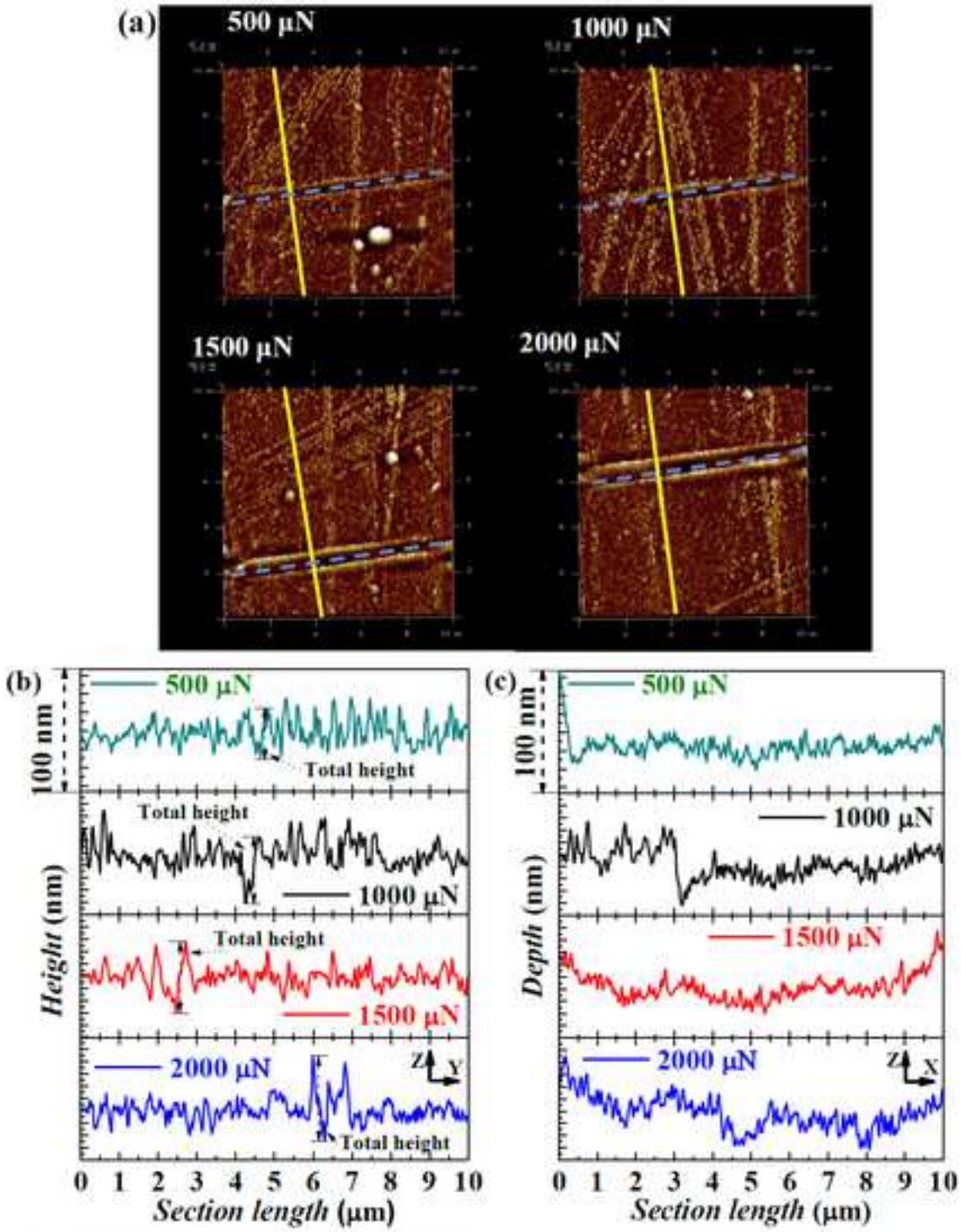

Fig. 5 Morphology of the scratch traces observed by AFM. (a) 3D morphologies of the scratch traces at four loading forces. (b) Profile of the cross-section along the yellow lines in (a). (c) Profile of the cross-section along the blue dashed line in (a). (d) Height and amplitude as functions of loading force.

Figure(s)
Click here to download high resolution image

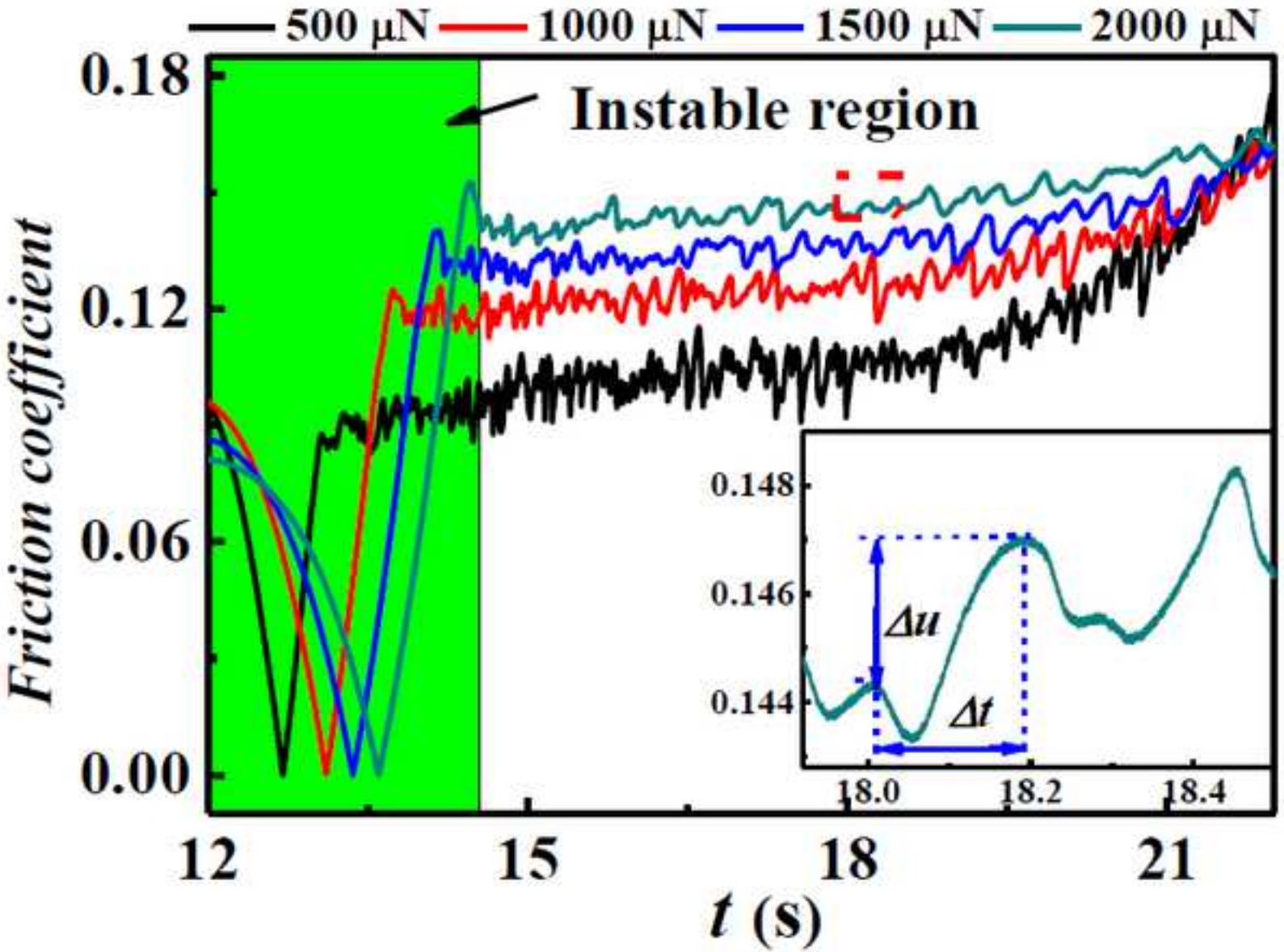

Fig. 6 Friction coefficient as a function of time. Inset shows the enlarged friction-coefficient–vs–time curve.

Figure(s)

Click here to download high resolution image

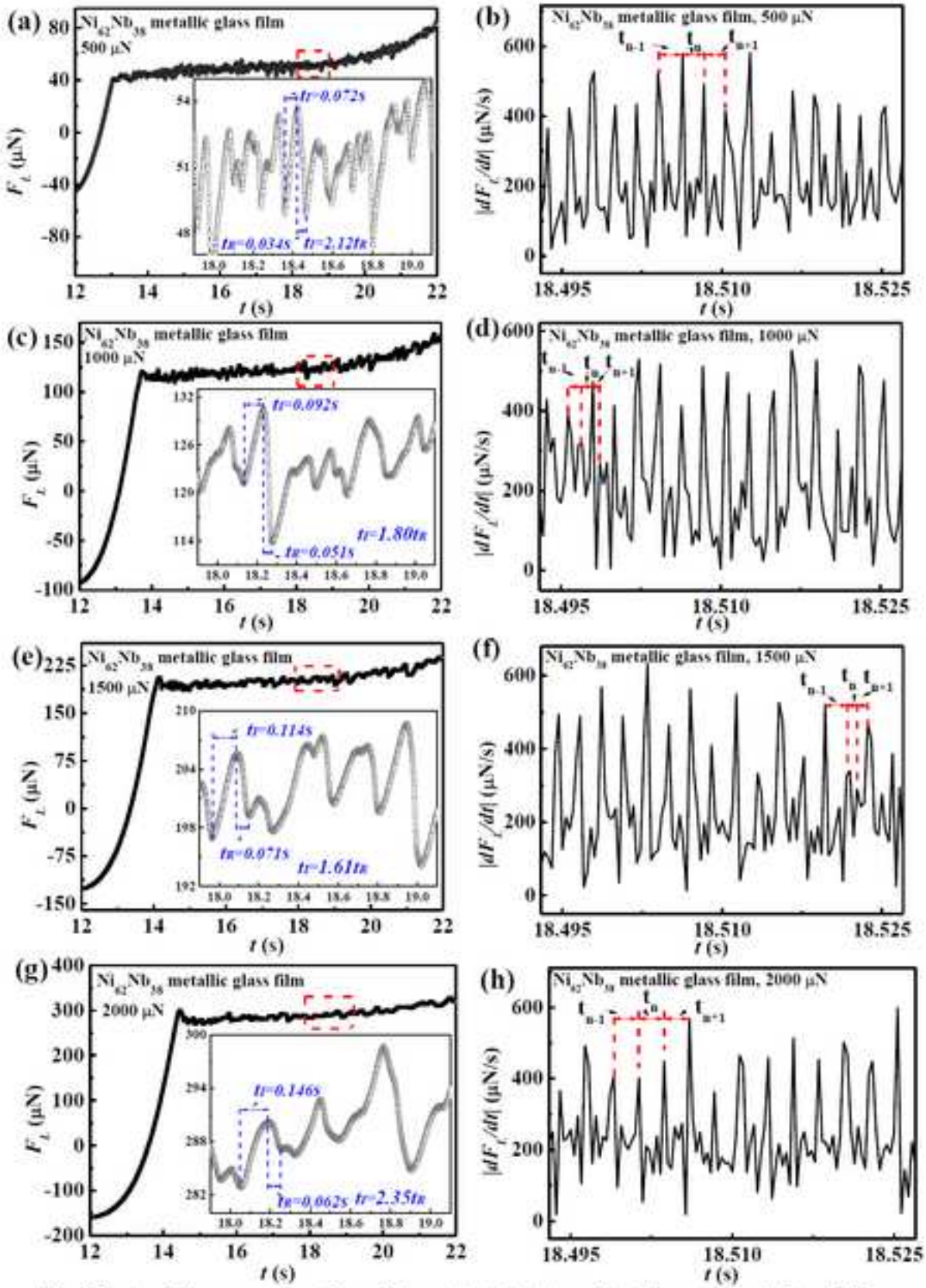

Fig. 7 Lateral force as a function of time. (a), (c), (e), and (g) show plots of lateral forces vs time at loading forces of 500, 1000, 1500, and 2000 μN, respectively. Insets show the enlarged lateral-force–vs–time curves. (b), (d), (f), and (h) present partial curves of $\left|\frac{dF_L}{dt}\right|$ vs time at loading forces of 500, 1000, 1500, and 2000 μN.

Figure(s)
Click here to download high resolution image

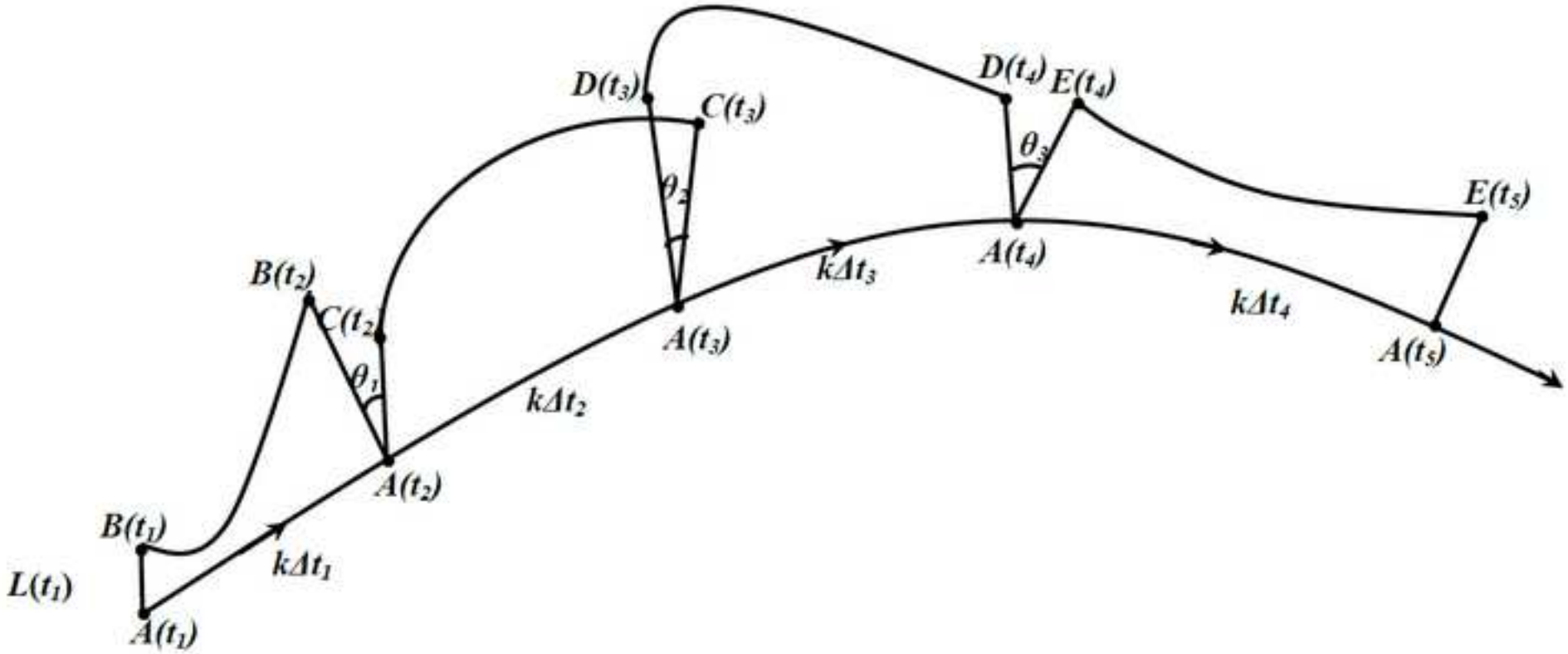

Fig. 8 Evolution of the phase-space trajectory.

Figure(s)
Click here to download high resolution image

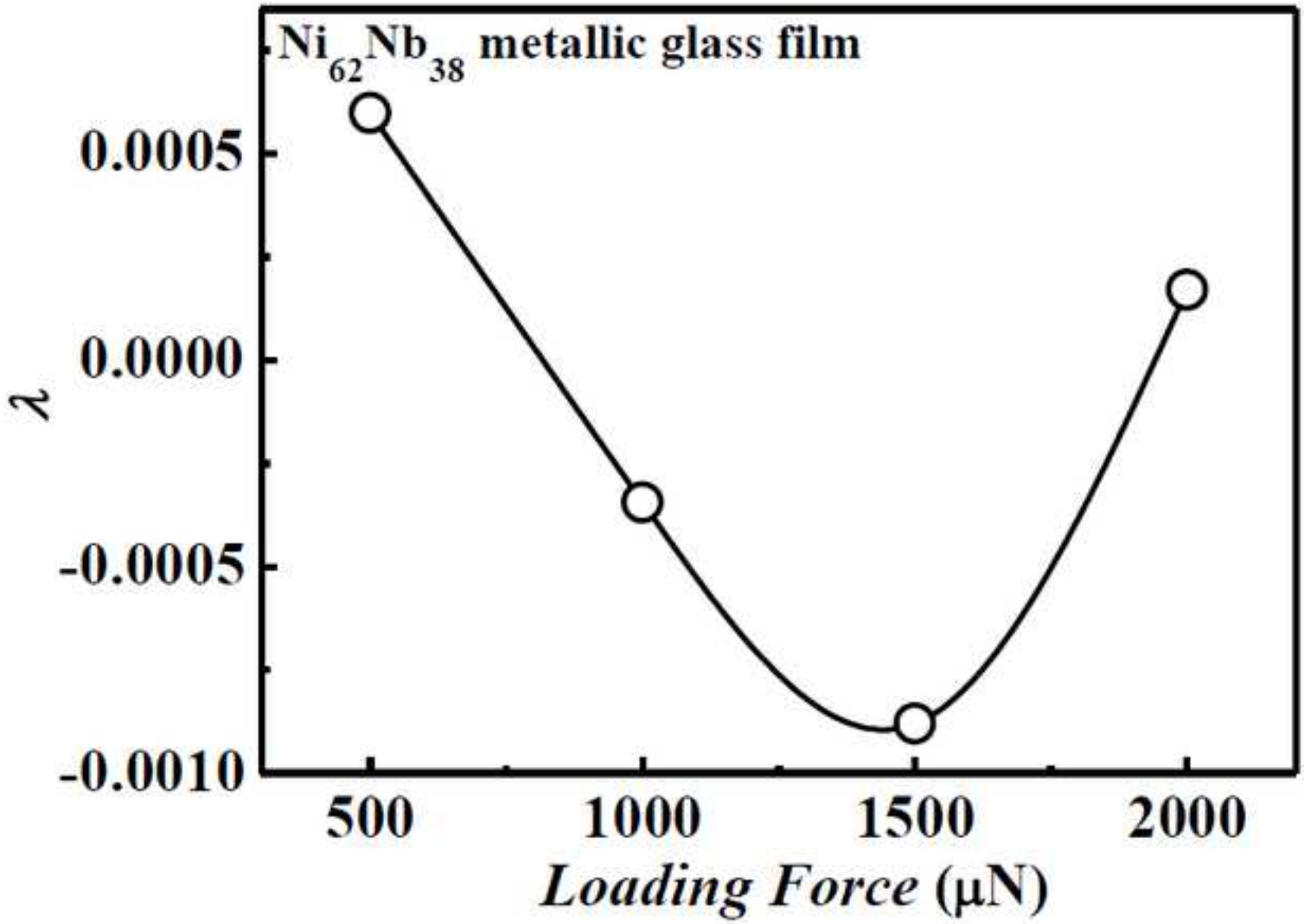

Fig. 9 Largest Lyapunov exponent as a function of loading force.

Figure(s)
Click here to download high resolution image

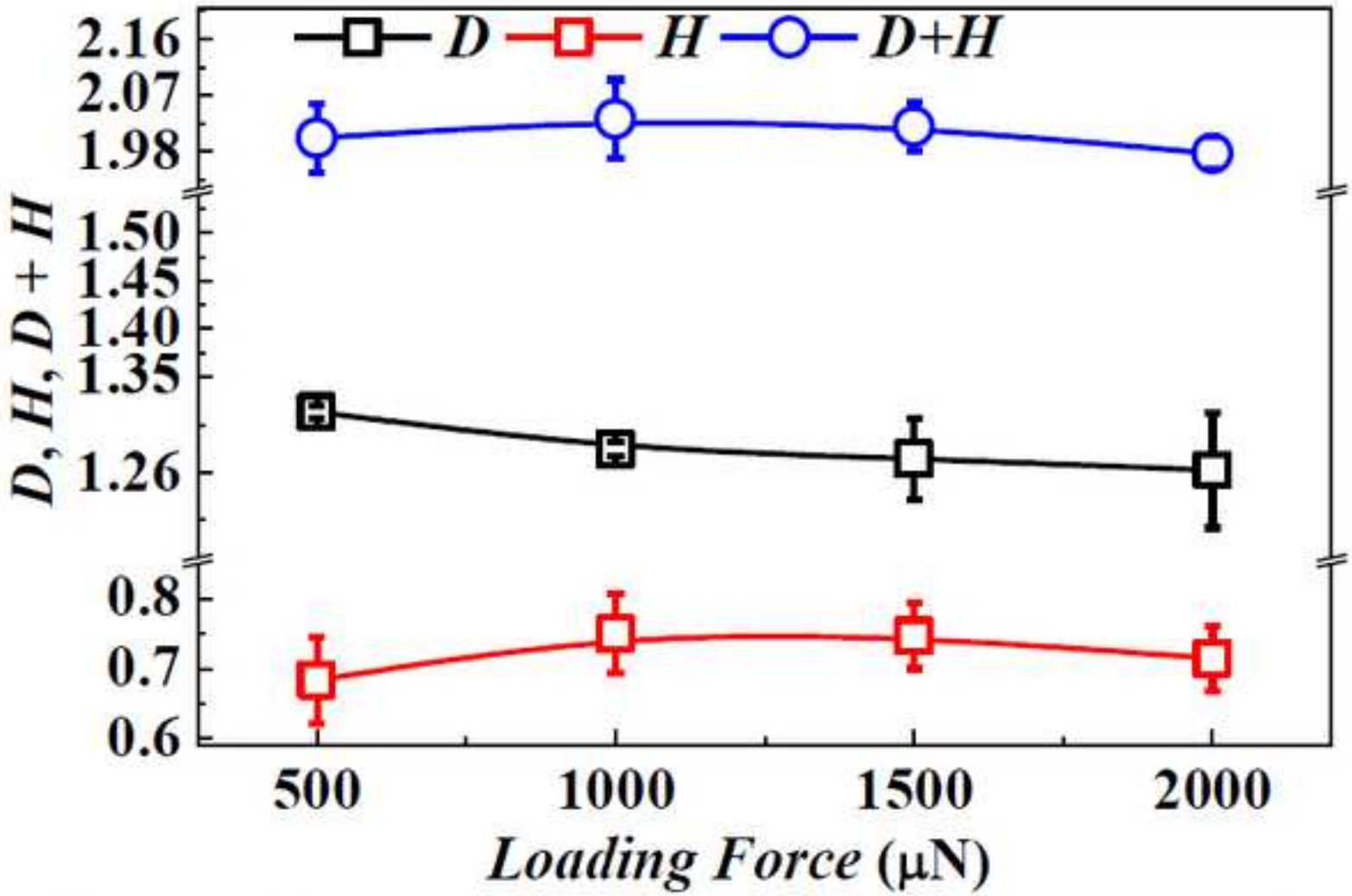

Fig. 10 Hurst exponent, *H*, fractal dimension, *D*, and *D*+*H* of $Ni_{62}Nb_{38}$ metallic glass film at loading forces of 500, 1000, 1500, and 2000 μN.

Figure(s)
Click here to download high resolution image

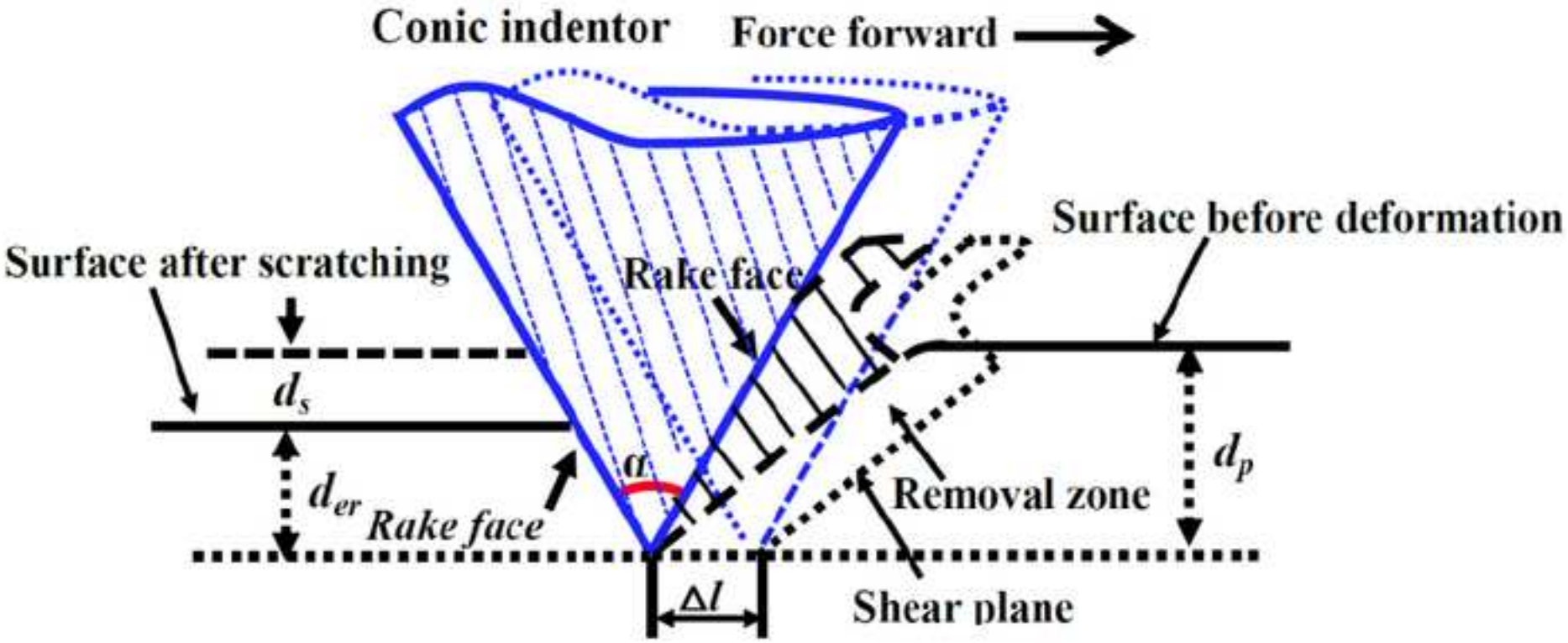

Fig. 11 Nanoscratching process. d_s is the scratch depth, d_{er} the elastic recover depth, α the angle of conic indentor [$\alpha=(\pi/3)$], Δl the unit scratch length, and d_p the penetration depth.

Figure(s)

Click here to download high resolution image

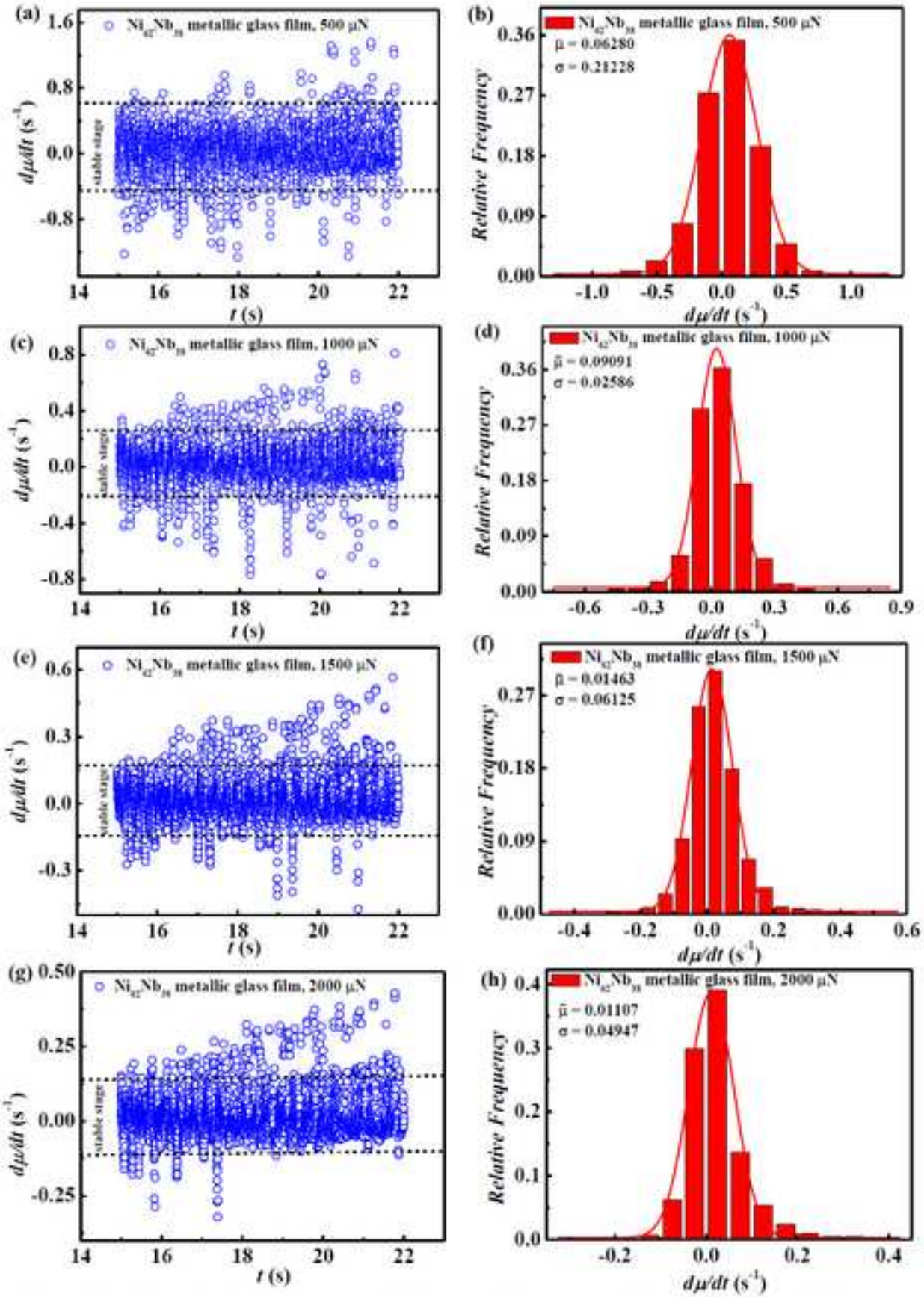

Fig. 12 Left-hand column, curves of differential friction coefficient vs time at different loading forces; right-hand column, curves of probability histogram of differential friction coefficient at different loading forces.

Supplementary Material

Click here to download Supplementary Material: supplementary information-21.docx

*Graphical Abstract